rotation. However, coronary arteries move and deform throughout the cardiac cycle, leading to degradation of image quality if temporal resolution is inadequate [6].

Temporal resolution is crucial for good image quality in CCTA [7, 8]. In order to improve temporal resolution, data from two or three cardiac cycles are used for image reconstruction which is called multi-segment reconstruction. When the gantry rotation time is 350 ms, temporal resolution of multi-segment reconstruction (MSR) images can be theoretically improved to 88 or 58 ms, respectively [9]. These are comparable to the temporal resolution of dual-source CT scanner (83 ms with single RR-cycle reconstruction and 42 ms with MSR algorithm) [10]. With some heart rates, benefits from improved temporal resolution with MSR might not offset the increased radiation dose and the decreased spatial resolution as the heart does not follow the same pattern of motion with every beat [8, 11]. Reconstruction algorithm that uses data from a single heart beat is called half-scan reconstruction algorithm. Although half-scan reconstruction (HSR) may result in lower radiation doses than MSR, images of patients with more rapid heart rate (HR) might be impaired due to the longer temporal resolution of HSR algorithm (approximately 175 ms when gantry rotation time is 350 ms).

There have been no studies that directly investigated coronary artery displacement and image quality in consecutive heart beats. Thus, the purpose of the present study was to investigate the influence of the beat-to-beat movement of the coronary arteries on image quality of MSR images.

Methods

Authors who are not employees of or consultants for Toshiba Medical Systems (Tokyo, Japan) had control of inclusion of any data and information that might present a conflict of interest for the author (R.T.), who is an employee of that company.

Patients

This retrospective study was approved by the local ethics committee, and the requirement for informed consent to participate this study was waived. In a retrospectively review, 23 consecutive patients (17 men, 6 women; mean age, 65.1 years ± 11.1; age range, 41–80 years) who underwent CCTA during November of 2009 were included in the analysis. All patients had clinical indications for CCTA and provided written informed consent for the examination. The patients were either suspected of having coronary artery disease (n = 18) or had a history of myocardial infarction with recurrent angina (n = 5). One patient with abnormal origin and course of a coronary artery was excluded from the study to minimize interfering factors affecting coronary artery motion. Four patients in whom the difference of R-R intervals exceeded 2% were also excluded in order to exclude the influence of HR variability. It is difficult to select the identical cardiac phase of the cardiac phase when R-R interval changes due to nonlinear changes in the time from the R wave to the various phases of the cardiac cycle as the heart rate varies [12]. We determined that 2% change of the R-R interval would have little influence on cardiac phase.

Thus the final study group included 18 patients (14 men, 4 women; mean age, 67.0 years ± 10.4; age range, 41–80 years) and a total of 21 exams.

CT data acquisition and postprocessing

All examinations were performed by using a 320-section CT scanner (Toshiba Aquilion ONE Dynamic Volume CT, Tochigi, Japan) with prospective ECG gating axial scans. The fraction of the R-R interval during which the patient was exposed ranged 65–85% for patients with lower HR [HR < 65 beats per minute (bpm)] and 30–80% for patients with higher HR (HR ≥ 65 bpm). The parameters were as follows: detector configuration, 320 × 0.5 mm; gantry rotation time, 350 or 375 ms depending on R-R time; tube potential, 120 kV; and tube current, ranging from 450 to 550 mA depending on body habitus. The effective radiation dose of CCTA was calculated as the product of the dose-length product times a conversion coefficient for the chest (k = 0.017 mSv/mGycm) [13]. Patients received 22.2 mgI/kg body weight/s of iopamidol 370 mgI/ml (Iopamiron 370, Bayer, Osaka, Japan, 54.6 ml ± 11.1; range, 38–79 ml) over 14 s. Bolus tracking in the ascending aorta was performed using a double threshold of 150 and 280 HU (Hounsfield unit). Patients were assigned to breathe in and hold their breaths after the first threshold. The scan

started just after the second threshold. Tatsugami et al. [14] showed that CCTA protocol using a double threshold yielded more consistent aortic enhancement with reduced interpatient variability than protocol using a single threshold.

One patient was receiving oral β-blocker as part of baseline medication. Oral β-blocker (20 mg of metoprolol) was indicated to 6 patients who had HR higher than 65 bpm at the outpatient department. The patients were assigned to take the medicine 2 h prior to the exam. No additional β-blocker was used when the HR was higher than 65 bpm at the time of the exam. There were no patients with contraindication to β-blockers, and there were no observed or reported side effects from β-blockers. All patients received 2.5 mg sublingual isosrobide dinitrate (Nitorol, Eisai, Tokyo, Japan) before imaging.

For each patient, the reconstruction phase with minimum artifact was determined at the CT console by reconstructing those 10 ms intervals available. Each exam contained three sets of images: HSR image of the first heart beat, HSR image of the second heart beat, and a two-beat MSR image.

CT data analysis

For data analysis, coronary segments were defined according to AHA guidelines [15]. Nine landmarks were identified in all reconstructed images (Fig. 1) and a multi-planar reconstruction image was generated on a cross-sectional plane for each landmark. Measurements were manually made by positioning a circular region of interest (ROI) and the x- and y-coordinates of the centroid of the circular ROI and the diameter were recorded. The ROI was placed three times and the average coordinates were used for evaluation. From these coordinates, the displacement of coronary artery motion was geometrically calculated in each HSR image using the following equation: displacement = $\left(\{x[h_1] - -x[h_2]\}^2 + \{y[h_1] - -y[h_2]\}^2\right)^{1/2}$, where h_1 and h_2 represent each HSR image. The motion ratio of coronary arteries was calculated as the division of displacement by diameter. The process described above was performed by one radiologist (N.T.).

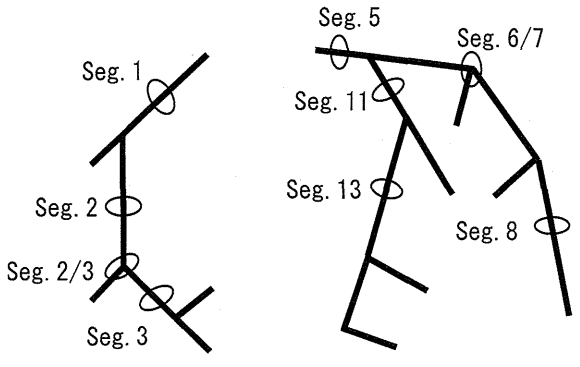

Fig. 1 Each landmark (*circle*) was identified at the mid-point of each segment. Nine landmarks were identified in all reconstructed images and a multi-planar reconstruction image was generated on a cross-sectional plane for each landmark

Image quality analysis

Two cardiovascular readers (N.T., S.·K.) independently rated coronary artery image quality. Before the reading session, the two readers determined by consensus image quality (IQ) scores defining the following four-point scale: 4, excellent, no artifact; 3, good, mild artifact; 2, acceptable, moderate artifact present but images still interpretable; 1, unable to evaluate, severe artifact renders interpretation not possible (Fig. 2). In the reading session, coronary arteries were shown patient by patient. For each patient, images were sorted in the order of coronary segment number in AHA guidelines. The three images of each landmark (2 HSR images and 1 MSR image) were displayed one by one randomly. The readers were blinded whether the images they were shown were HSR or MSR. When there was a difference in IQ scores between the two readers, the final IQ score was determined by consensus.

When the IQ score of at least one of the two HSR images was better than the score of MSR image, we defined HSR image better than MSR image (group A). Image quality of MSR image was considered better than that of HSR images when the IQ score of the MSR image was better than the scores of both HSR images (group C). Otherwise, image quality was considered equivalent (group B).

Statistical analysis

All statistical analyses were performed with commercially available statistical software (JMP, version 8.0.2; SAS, Cary, NC). Quantitative variables were expressed as means ± standard deviation.

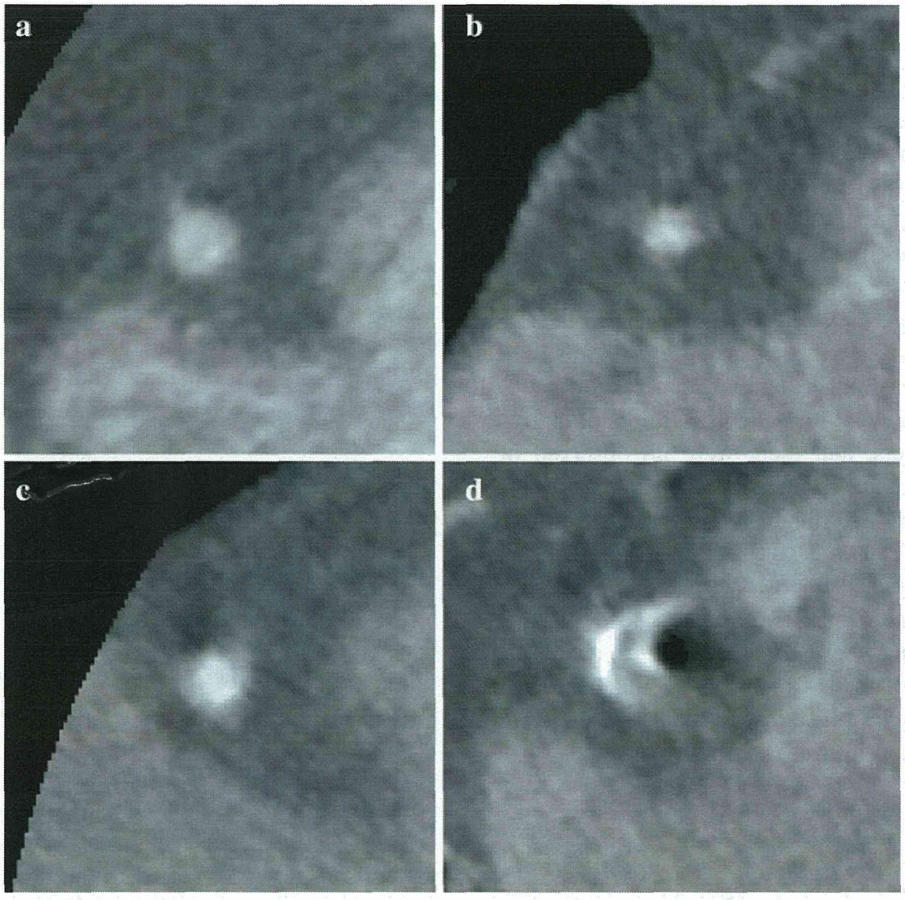

Fig. 2 Representative images through the mid-RCA illustrate the four image quality scores. 4, Excellent, no artifact (**a**); 3, Good, mild artifact (**b**); 2, Acceptable, moderate artifact present but images still interpretable (**c**); 1, Unable to evaluate, severe artifact renders interpretation not possible (**d**). Before the reading session, the two readers determined by consensus image quality scores. *RCA* right coronary artery

Interobserver agreement for image quality was calculated with Cohen κ statistics [16]. Result was interpreted as poor ($\kappa < 0.20$), fair ($\kappa = 0.21$–0.40), moderate ($\kappa = 0.41$–0.60), good ($\kappa = 0.61$–0.80), very good ($\kappa = 0.81$–0.90), or excellent ($\kappa \geq 0.91$).

The difference between the average IQ scores of HSR and MSR images of all exams was assessed by Welch's t test. Correlation of the motion ratio to HR, body mass index (BMI) and total body weight was analyzed by Spearman's rank-order correlation coefficients. The significance level was adjusted by Bonferroni to $0.05/3 = 0.017$. Correlation of MSR IQ score to the displacement and the motion ratio was also analyzed by Spearman's rank-order correlation coefficients. The significance level was adjusted by Bonferroni to $0.05/2 = 0.025$. The difference of the motion ratio between groups A–C was assessed by Steel–Dwass' test. Fisher's exact test was used to assess the frequency of the HSR IQ score difference between group A and groups B and C.

Results

Mean heart rate during scanning was 67.0 bpm ± 10.4 (range 51–89 bpm). The estimated mean dose-length product and the mean effective radiation dose was 918 mGycm ± 376 and 15.6 mSv ± 6.4 each.

Motion of coronary artery segments

Four of the possible 189 segments (21 exams × 9 segments per exam) were either not present (n = 1)

Table 1 Summary of average displacement, diameter, and motion ratio in each coronary artery segment

Coronary segment	Displacement (mm)	Diameter (mm)	Motion ratio (%)
#1	0.60 ± 0.36	4.2 ± 0.7	14 ± 7
#2	0.63 ± 0.31	4.0 ± 0.6	16 ± 8
#2/3	0.65 ± 0.41	3.5 ± 0.7	20 ± 15
#3	0.64 ± 0.48	3.1 ± 0.8	21 ± 15
#5	0.48 ± 0.30	4.7 ± 1.1	11 ± 8
#6/7	0.38 ± 0.21	3.7 ± 0.7	11 ± 8
#8	0.49 ± 0.39	2.3 ± 0.3	22 ± 16
#11	0.50 ± 0.51	3.5 ± 0.7	16 ± 19
#13	0.44 ± 0.38	2.4 ± 0.7	20 ± 20

Data are average ± standard deviations

or poorly imaged due to a stent inside (n = 1) or occluded (n = 2) limiting measuring coordinates. A summary of average displacement, diameter and the motion ratio is shown in Table 1. There was no significant relationship between average motion ratio and HR (r = 0.17; $P = 0.47$), BMI (r = 0.057; $P = 0.80$) and total body weight (r = 0.07; $P = 0.77$) for each exam.

Image quality of coronary artery segments

Interobserver agreement was interpreted as "very good" ($\kappa = 0.82$). Four of the possible 189 segments were either occluded (n = 2), had a stent inside (n = 1), or were not present (n = 1), limiting evaluation.

For MSR images, images without artifacts (score 4) were obtained in 103 segments (55.7%); images with mild artifacts (score 3) in 64 segments (34.6%); images with moderate artifacts (score 2) in 14 segments (7.6%); and images with severe artifacts (score 1) in 4 segments (2.2%). For HSR images, 196 segments (53.0%) were rated as score 4, 121 segments (32.7%) as score 3, 42 segments (11.4%) as score 2, and 11 segments (3.0%) as score 1.

IQ scores of HSR and MSR images on a per-segment basis are shown in Table 2. Average IQ scores were not significantly different ($P = 0.28$) between HSR and MSR images. There was a significant negative correlation between MSR IQ score and the displacement of coronary artery segments (r = −0.36; $P = 0.018$) (Fig. 3a). The correlation between MSR IQ score and the motion ratio showed a stronger negative correlation (r = −0.54; $P = 0.0002$) (Fig. 3b).

Table 2 IQ scores of MSR and HSR images on a per-segment basis

Coronary segment	MSR IQ score	HSR IQ score
#1	3.8 ± 0.4	3.5 ± 0.7
#2	3.0 ± 0.7	2.9 ± 0.9
#2/3	3.2 ± 0.9	3.3 ± 0.9
#3	3.4 ± 0.7	3.4 ± 0.7
#5	3.8 ± 0.4	3.8 ± 0.5
#6/7	3.7 ± 0.6	3.6 ± 0.6
#8	3.1 ± 0.8	3.0 ± 0.9
#11	3.7 ± 0.6	3.6 ± 0.6
#13	3.3 ± 0.8	3.1 ± 0.8
Average	3.4 ± 0.7	3.4 ± 0.8

Data are average ± standard deviations

IQ image quality, *MSR* multi-segment reconstruction, *HSR* half-scan reconstruction

Thirty-seven segments (20.0%) were included in group A, 133 segments (71.9%) in group B and 15 segments (8.1%) in group C. Of the 109 segments in which the IQ scores of the two HSR images were equivalent, 14 segments (12.8%) were included in group A, 85 segments (78.0%) in group B and 10 segments (9.2%) in group C.

Effect of motion ratio on image quality

The motion ratio for group A was 29.1% ± 17.3; that for group B was 13.5% ± 11.6; and that for group C was 16.0% ± 6.3. The motion ratio for group A was significantly larger than that for group B ($P < 0.05$). The motion ratio for all segments in group C was lower than 25% (Fig. 4).

Effect of difference in HSR IQ scores on MSR IQ score

Of the 151 segments in which the motion ratio was lower than 25%, 18 (11.9%) segments were included in group A. The HSR IQ scores were equivalent in 3 (16.7%) of the 18 segments. Of the remaining 133 segments, the HSR IQ scores were equivalent in 88 (66.0%) segments. Difference in IQ scores was more frequent in segments of group A than in the remaining segments in which the motion ratio was lower than 25% ($P < 0.0002$).

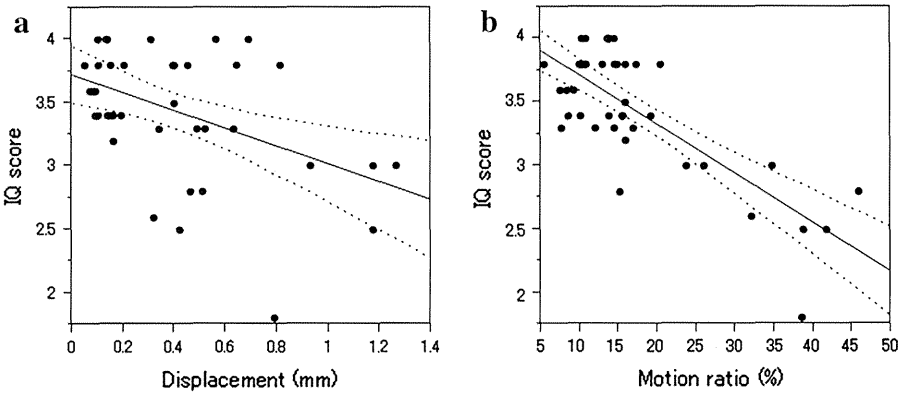

Fig. 3 Scattergram shows relationship between MSR IQ score and the movement of the coronary arteries. *Solid lines* show linear regression. *Dotted lines* represent 95% confidence limits. Each plot represents the average value of RCA (#1, #2, #2/3, #3) and LCA (#5, #6/7, #8, #11, #13) in each exam. Correlation between MSR IQ score and the displacement was −0.36 ($P = 0.018$), indicating statistically significant negative correlation (**a**). However, the correlation between MSR IQ score and the motion ratio was −0.54 ($P = 0.0002$), indicating stronger negative correlation than the correlation between MSR IQ score and displacement (**b**). The motion ratio would be a better index to evaluate the effect of the motion of coronary arteries on image quality. *MSR* multi-segment reconstruction, *IQ* image quality, *RCA* right coronary artery, *LCA* left coronary artery

Discussion

Rapid motion of the heart degrades the image quality of coronary arteries in CCTA [7]. The present study showed that there was a negative relationship between MSR IQ score and the displacement of coronary arteries in consecutive two beats. However, the negative relationship was stronger between MSR IQ score and the motion ratio. The motion ratio is calculated by dividing the displacement by the diameter of the coronary artery segment, such that smaller coronary artery segment has a higher motion ratio when the absolute displacement is the same. The results in the present study show that the image quality of smaller segments could be more vulnerable to cardiac motion. Thus we used the motion ratio as an index to evaluate the effect of the motion of coronary arteries on image quality.

The present study showed that IQ scores of MSR images would be degraded when the motion ratio is above 25%. Although the average motion ratio was higher in group A than in group C, the difference was not significant. The reason for this could be because the difference in the image quality of HSR images could also impair the image quality of MSR images as discussed later. However, we could not find a relationship between motion ratio and HR, BMI and total body weight. Sebastian et al. [17] showed a strong correlation between variability (i.e., standard deviation) of HR during scanning and mean image quality. Their study showed that image quality was significantly better in patients with low variability in HR. In the present study, patients were included whose variability of R-R interval was lower than 2%; hence, further investigation is required to find relationship between the motion ratio and variability of R-R intervals. It is difficult to know beforehand which factor causes a higher motion ratio.

Even when the motion ratio was lower than 25%, 11.9% of all segments were included in group A. The difference in IQ scores in HSR images in a single segment was more frequent in segments which were included in group A when the motion ratio was lower than 25% than in the remaining segments in which the motion ratio was lower than 25%. Thus, image quality of MSR images might be degraded when one of the HSR images is impaired. It is clinically known that there are nonlinear changes in the time from the R wave to the various phases of the cardiac cycle as the heart rate varies (i.e., the diastolic phases are more sensitive to changes in heart rate than systole) [12]. However, the cardiac phase would be the same when the R-R interval is unchanged. The present results imply that cardiac phase might change even if heart rates do not change. There might be other causes which could lead to the difference of IQ scores. During acquisition of the latter beat, residual contrast agent in the right ventricle decreases

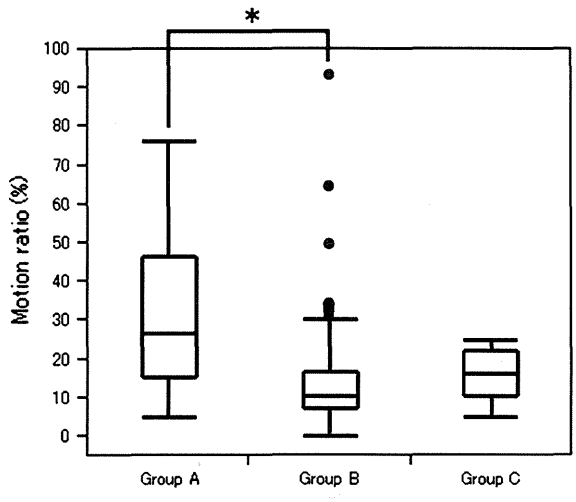

Fig. 4 When the IQ score of at least one of the two HSR images was better than the score of MSR image, we defined HSR image better than MSR image (group A). Image quality of MSR image was considered better than that of HSR images when the IQ score of the MSR image was better than the scores of both HSR images (group C). Otherwise, image quality was considered equivalent (group B). All plots in group C were lower than 25%, thus IQ scores of MSR images would be degraded when the motion ratio is above 25%. Although the average motion ratio was higher in group A than in group C, the difference was not significant. The reason for this could be because the difference in the image quality of HSR images could also impair the image quality of MSR images. Note *Box* 1st–3rd quartiles, *bold line* median, *whiskers* minimum and maximum values, *filled circle* outlier, *asterisk* statistically significant ($P < 0.05$). *IQ* image quality, *HSR* half-scan reconstruction, *MSR* multi-segment reconstruction

compared to the former beat. Horiguchi et al. [18] showed that heart rate varies immediately after breath hold and that 4 or 5 s after breath hold is recommended before starting cardiac CT examination. Further study is necessary to investigate whether these factors have influence on image quality of the HSR images.

The present study does not suggest MSR has no advantage and therefore should be avoided in this 320-slice CT scanner. Previous studies have shown that MSR improves image quality in higher heart rates [8, 19, 20]. In the present study, the image quality was equivalent with HSR and MSR images in 71.9% of all segments. The reason for this could be because the average HR was 67.0 bpm. Herzog et al. [19] showed that MSR benefits only at certain heart rates. This is because the time resolution oscillates between half and quarter of the gantry rotation time depending on heart rate [10, 19, 21]. Herzog et al. used the same helical pitch and gantry rotation time in all patients, hence the heart rate in which the MSR benefits was limited. The time resolution of MSR could be improved in various heart rates by changing the gantry rotation time in 320-detector CT with heart rate of each patient. The present study showed that motion of coronary arteries could also impair MSR image quality. Further study is needed to investigate the factor which causes higher movement of coronary arteries thus improving the image quality of MSR images.

There were some limitations in this study. By employing a limited number of landmarks on coronary arteries, we have provided descriptions of coronary artery motion only at selected points. However, motion of coronary arteries is non-uniform and is characterized by changes in the magnitude and direction of vessel motion and axial strain [22, 23].

A third of this study population was receiving β-blocker medications. Therefore, in the present study population, actual coronary movements may have been underestimated. Patients with various degrees of cardiac disease were included. The degree of impairment in ventricular motion caused by myocardial disease would lead to deviations of the motion patterns.

This study was restricted in two-dimensional analysis. Coronary artery segments were assessed on a single plane. Coronary arteries move in a three-dimensional way; thus, the present data do not show the exact movement of each segment. In order to assess the movement for each segment, bifurcation points need to be identified as landmarks.

Finally, the time resolution for MSR images was not analyzed. By using two-beat MSR, temporal resolution oscillates between one-half and one-fourth of the gantry rotation time, depending on the heart rate [11, 21].

In conclusion, the motion ratio could be a better index than the displacement to evaluate the influence of the motion of coronary arteries on image quality. MSR images would be impaired by a motion ratio larger than 25%. Image impairment of one of the HSR images might also impair MSR images. However, there was no significant relationship between the motion ratio and HR, BMI and total body weight. Further study is necessary to investigate factors which may influence on the movement in consecutive heart beats.

Acknowledgments We have not received any funding for this study.

References

1. Hendel RC, Kramer CM, Patel MR, Poon M (2006) ACCF/ACR/SCCT/SCMR/ASNC/NASCI/SCAI/SIR 2006 Appropriateness criteria for cardiac computed tomography and cardiac magnetic resonance imaging. A report of the American College of Cardiology Foundation Quality Strategic Directions Committee Appropriateness Criteria Working Group, American College of Radiology, Society of Cardiovascular Computed Tomography, Society for Cardiovascular Magnetic Resonance, American Society of Nuclear Cardiology, North American Society for Cardiac Imaging, Society for Cardiovascular Angiography and Interventions, and Society of Interventional Radiology. J Am Coll Cardiol 48:1475–1497
2. Vanhoenacker PK, Heijenbrok-Kal MH, Van Heste R et al (2007) Diagnostic performance of multidetector CT angiography for assessment of coronary artery disease: meta-analysis. Radiology 244:419–428
3. Scheffel H, Alkadhi H, Plass A et al (2006) Accuracy of dual-source CT coronary angiography: first experience in a high pre-test probability population without heart rate control. Eur Radiol 16:2739–2747
4. Mollet NR, Cademartiri F, van Mieghem CA et al (2005) High-resolution spiral computed tomography coronary angiography in patients referred for diagnostic conventional coronary angiography. Circulation 112:2318–2323
5. Dewey M, Zimmermann E, Deissenrieder F et al (2009) Noninvasive coronary angiography by 320-row computed tomography with lower radiation exposure and maintained diagnostic accuracy. Circulation 120:823–824
6. Ding Z, Friedman MH (2000) Quantification of 3-D coronary arterial motion using clinical biplane cineangiograms. Int J Card Imaging 16:331–346
7. Achenbach S. (2007) CT coronary angiography. Half-Scan vs. multi-segment reconstruction for computed tomography coronary angiography. SOMATOM Sessions. http://www.medical.siemens.com/siemens/en_US/cs_cardio_FBAs/files/Case_Study/Achenbach_MultiSegment_Reconstruction.pdf. Accessed 4 September 2010
8. Halliburton SS, Stillman AE, Flohr T et al (2003) Do segmented reconstruction algorithms for cardiac multislice computed tomography improve image quality? Herz 28:20–31
9. Kitagawa K, Lardo AC, Lima JAC, George RT (2009) Prospective ECG-gated 320 row detector computed tomography: implications for CT angiography and perfusion imaging. Int J Cardiovasc Imaging 25:201–208
10. Achenbach S, Ropers D, Kuettner A et al (2006) Contrast-enhanced coronary artery visualization by dual-source computed tomography—initial experience. Eur J Radiol 57:331–335
11. Flohr T, Ohnesorge B (2001) Heart rate adaptive optimization of spatial and temporal resolution for electrocardiogram-gated multislice spiral CT of the heart. J Comput Assist Tomogr 25:907–923
12. Vembar M, Garcia MJ, Heuscher DJ et al (2003) A dynamic approach to identifying desired physiological phases for cardiac imaging using multislice spiral CT. Med Phys 30:1683–1693
13. Einstein AJ, Moser KW, Thompson RC et al (2007) Radiation dose to patients from cardiac diagnostic imaging. Circulation 116:1290–1305
14. Tatsugami F, Matsuki M, Shigesato H et al. A new imaging technique using real prep with 320 detector coronary CT angiography [article in Japanese]. Paper presented at: Meeting of Japan Society of Cardiovascular Radiology, Kumamoto, Japan, 3 July 2010
15. Austen WG, Edwards JE, Frye RL et al (1975) A reporting system on patients evaluated for coronary artery disease: report of the Ad Hoc Committee for grading of coronary artery disease, council on cardiovascular surgery, American Heart Association. Circulation 51:5–40
16. Cohen J (1960) A coefficient of agreement for nominal scales. Educ Pshychol Meas 20:37–46
17. Leschka S, Wildermuth S, Boehm T et al (2006) Noninvasive coronary angiography with 64-section CT: effect of average heart rate and heart rate variability on image quality. Radiology 241:378–385
18. Horiguchi J, Yun S, Hirai N et al (2006) Timing on 16-slice scanner and implications for 64-slice cardiac CT: do you start scanning immediately after breath hold? Acad Radiol 13:173–176
19. Herzog C, Nguyen SA, Savino G et al (2007) Does two-segment image reconstruction at 64-section CT coronary angiography improve image quality and diagnostic accuracy? Radiology 244:121–129
20. Wang YT, Yang CY, Hsiao JK et al (2009) The influence of reconstruction algorithm and heart rate on coronary artery image quality and stenosis detection at 64-detector cardiac CT. Korean J Radiol 10:227–234
21. Ebert TJ, Eckberg DL, Vetrovec GM et al (1984) Impedance cardiograms reliably estimate beat-by-beat changes of left ventricular stroke volume in humans. Cardiovasc Res 18:354–360
22. Ding Z, Friedman MH (2000) Dynamics of human coronary arterial motion and its potential role in coronary atherogenesis. J Biomech Eng 122:488–492
23. Duerinckx A, Atkinson DP (1997) Coronary MR angiography during peak-systole: work in progress. J Magn Reson Imaging 7:979–986

Journal of Cardiovascular Computed Tomography (2012) 6, 318–324

Journal of Cardiovascular Computed Tomography

Original Research Article

Adaptive Iterative Dose Reduction in coronary CT angiography using 320-row CT: Assessment of radiation dose reduction and image quality

Nobuo Tomizawa, MD[a,*], Takeshi Nojo, MD[a], Masaaki Akahane, MD[a], Rumiko Torigoe, RT[b], Shigeru Kiryu, MD[c], Kuni Ohtomo, MD[a]

[a]Department of Radiology, The University of Tokyo, 7-3-1 Hongo, Bunkyo-ku, Tokyo 113-0033, Japan; [b]Toshiba Medical Systems Corporation, Tokyo Metropolitan Regional Office, Tokyo, Japan and [c]Department of Radiology, Institute of Medical Science, The University of Tokyo, Tokyo, Japan

KEYWORDS:
Coronary CT angiography;
Effective dose;
Filtered back projection;
Iterative reconstruction;
320-row CT

BACKGROUND: Several methods have been developed to reduce the radiation dose in coronary computed tomography angiography (CTA).

OBJECTIVE: The objective of our study was to evaluate the effects of Adaptive Iterative Dose Reduction (AIDR) on objective and subjective image quality as well as the radiation dose, compared with conventional filtered back projection (FBP), in coronary CTA.

METHODS: We retrospectively reviewed 100 consecutive patients who underwent coronary CTA. In the first 50 patients, a higher tube current was used, and images were reconstructed with FBP. In the last 50 patients, a lower tube current was used, and images were reconstructed with AIDR. Subjective and objective image quality (noise, signal-to-noise ratio, contrast-to-noise ratio) were assessed.

RESULTS: The median radiation dose of the AIDR group was 22% lower than that of the FBP group (4.2 vs 5.4 mSv; $P = 0.0001$). No significant difference was found in subjective image quality, noise, signal-to-noise ratio, or contrast-to-noise ratio between the 2 groups.

CONCLUSION: AIDR reduced the tube current which resulted in reduction of radiation dose in coronary CTA while maintaining subjective and objective image quality compared with coronary CTA reconstructed with FBP.

Introduction

Significant advances in coronary computed tomography angiography (CTA) have allowed noninvasive evaluation of the heart and coronary arteries.[1] Coronary CTA requires high spatial resolution and low noise, which are accomplished with various radiation doses across patients and imaging facilities (1−20 mSv).[2] Several methods have been developed to reduce the radiation dose to meet the "as low as reasonably achievable principle" for coronary CTA.[2,3] These methods include electrocardiogram-based tube current modulation for helical examinations,[2–5] prospective gating,[2,4,5] noise reduction filters,[4] high-pitch spiral acquisition,[2,5] reduction of tube voltage,[2,3,5] and reduction of z-axis scan length.[2,3]

Conflict of interest: The authors report no conflicts of interest.

* Corresponding author.
E-mail address: tomizawa-tky@umin.ac.jp

Submitted November 13, 2011. Accepted for publication February 27, 2012.

1934-5925/$ - see front matter © 2012 Society of Cardiovascular Computed Tomography. All rights reserved.
http://dx.doi.org/10.1016/j.jcct.2012.02.009

Filtered back projection (FBP) algorithms are currently the most widespread technique for reconstruction in CT.[6] FBP is based on the back projection of attenuation line integrals acquired from radial views that covers within the patient. The main advantage of the FBP includes fast reconstruction speed; however, the main disadvantage is the overall limitations in image quality, mainly because of the back-projection process and the necessary filtering, which accentuates noise and can result in streak artifacts.

Noise-reducing statistical iterative reconstruction algorithms can be used to decrease x-ray exposure.[6,7] Adaptive Iterative Dose Reduction (AIDR; Toshiba Medical Systems, Tokyo, Japan) is an iterative algorithm designed to work in both raw data and reconstruction domains.[8] This is unlike Iterative Reconstruction in Image Space (IRIS; Siemens Medical Solutions, Malvern, PA) which uses image data only[4,6] or Model-based Iterative Reconstruction (GE Healthcare, Waukesha, WI) which uses raw data only.[6]

Lowering the x-ray exposure and therefore reducing the number of photons reaching the detector results in a decrease in signal-to-noise ratio (SNR) in raw data. The AIDR algorithm first analyses the noise in the raw data and then adaptively applies noise correction based on the photon count. This process in effect increases the SNR, particularly with low-dose acquisitions. After raw data noise correction is applied, a primary reconstruction is performed. AIDR uses an iterative data enhancement algorithm in the reconstruction domain. This algorithm adapts to different organs which maximizes the noise reduction without compromising spatial resolution. The final process involves a weighted blending of the iterative and the primary reconstruction to create the AIDR image. As a result of this blending, the AIDR images retain a natural appearance as if they were acquired with standard exposure parameters.

Gervaise et al[9] showed that AIDR significantly improved image quality in CT examinations of the lumbar spine and has the potential to decrease radiation dose. However, clinical capabilities of AIDR in coronary CTA have not been studied. Our hypothesis was that AIDR would permit CTA with reduced radiation dose while preserving study interpretability. The objective of our study was to evaluate the effects of AIDR on objective and subjective image quality as well as the radiation dose, compared with conventional FBP, in coronary CTA with the use of 320-row CT.

Methods

This retrospective study was approved by the local ethics committee, and the requirement for informed consent to participate in this study was waived.

Patients

Power analysis was performed to determine the minimum cohort size. Our hypothesis was that per-segment subjective image quality would be similar between groups. To detect a difference of 0.1 in subjective image quality score, the minimum sample size was determined to be a total of 450 segments (approximately 30 patients) at 0.8773 power; sample size calculations were based on a type 2 error ($\alpha = 0.05$).

The records of 112 consecutive patients (71 men and 41 women; age, 66.1 ± 10.5 years; age range, 24–85 years; body weight [BW], 63.2 ± 13.1 kg; BW range, 35–124 kg) who underwent coronary CTA from June to September 2011 were retrospectively examined. The patients with several risk factors of coronary artery disease with chest pain and/or dyspnea and abnormal results of electrocardiogram, cardiac echo, or treadmill test were included in our study. Seven patients who received a wide volume scan to evaluate bypass grafts and 1 patient with a BW of 124 kg were excluded from the examination because a longer (≥17 seconds) contrast injection protocol was used. Three patients who had congenital heart disease and 1 patient with intense calcification in all 3 coronary arteries, which limited the image quality evaluation, were excluded. The final study group included 100 patients (61 men and 39 women; age, 67.2 ± 9.6 years; age range, 36–85 years; BW, 62.5 ± 11.6 kg; BW range, 35–94 kg). From June 2011 to July 2011, 50 patients underwent CTA with FBP reconstruction (group 1). After AIDR was available in August 2011, the tube current was reduced for the last 50 patients receiving CTA (group 2). The AIDR version we used was AIDR 3D. The patient demographics are described in Table 1.

CT data acquisition

All examinations were performed with a 320-row CT scanner (Aquilion ONE Dynamic Volume CT; Toshiba,

Table 1 Patient demographics and scanning parameters

Parameter	Group 1	Group 2	*P*
Number of patients	50	50	
Male/female	32/18	29/21	0.68
Age (y)	68.8 ± 9.5	65.6 ± 9.6	0.10
BW (kg)	62.6 ± 11.2	62.4 ± 11.3	0.94
BMI (kg/m^2)	24.0 ± 3.0	23.9 ± 3.7	0.90
β-Blocker	30	33	0.70
HR (beats/min)	64.0 ± 11.2	64.6 ± 11.8	0.78
Injection rate (mL/s)	3.7 ± 0.7	3.7 ± 0.7	0.80
Tube current (mA)	483 ± 93	289 ± 74	<0.0001*
Heartbeats for acquisition			0.67
1 beat	28	25	
≥2 beats	22	25	
Scan length (cm)	13.6 ± 1.3	13.2 ± 1.3	0.10

BW, body weight; BMI, body mass index; HR, heart rate.
*The significance level was adjusted by the Bonferroni method to $P < 0.005$.

Tochigi, Japan) with prospectively electrocardiogram-triggered axial scans. The heart was reconstructed with 1 heartbeat when the heart rate (HR) was ≤65 beats/min, with 2 heartbeats when HR was between 65 and 80 beats/min, and with 3 heartbeats when HR was >80 beats/min. The acquisition window was set at 70%−85% of the R–R interval in patients with HR <60 beats/min; 65%−85% in patients with HR between 60 and 70 beats/min; and 30%−80% in patients with HR ≥70 beats/min.

The scanning parameters were as follows: detector configuration of 320 × 0.5 mm; rotation time of 350, 375, or 400 milliseconds depending on HR; and tube potential of 120 kV. The tube current was determined by the BW. The tube current in group 1 was set at 270 mA in patients with BW <50 kg; 450 mA with BW 50−59 kg; 500 mA with BW 60−69 kg; and 550 mA with BW ≥70 kg. The tube current in group 2 was set at 200 mA in patients with BW <50 kg; 250 mA with BW 50−59 kg; 270 mA with BW 60−69 kg; 400 mA with BW 70−79 kg; 450 mA with BW 80−89 kg; 500 mA with BW 90−99 kg; and 550 mA with BW ≥100 kg. We calculated the tube current for group 2 on the basis of the noise of group 1 and the reduction of noise with the use of strong AIDR algorithm compared with FBP algorithm to achieve a noise of approximately 22 HU. The focal spot size of the x-ray source in this scanner was automatically selected, depending on the tube current. When the tube current was 270 mA or less, a small focal spot size was used, and when the tube current was larger than 270 mA, a large focal spot size was used. The mean effective dose was derived from the dose length product (DLP) multiplied by a conversion coefficient for the chest (κ = 0.014 mSv × mGy^{-1} × cm^{-1}).[10] The scan length ranged from 12 to 16 cm, depending on the size of the heart.

The patients received 22.2 mg I/kg per second of iopamidol 370 mg I/mL (Iopamiron 370; Bayer, Osaka, Japan; mean volume administered, 51.9 ± 9.7 mL; range, 29−79 mL) for 14 seconds. The patients underwent bolus tracking in the descending aorta, using a double threshold of 100 and 290 HU. Patients were assigned to breathe in and hold their breath after the first threshold. The scan started after the second threshold. Compared with the single threshold protocol, the double threshold protocol for coronary CTA yielded more consistent aortic enhancement with reduced interpatient variability.[11]

Twenty-nine patients were receiving an oral β-blocker as part of baseline medication, and an oral β-blocker (20−40 mg of metoprolol or propranolol) was administered to 39 outpatients with HR >65 beats/min. The patients were told to take the medicine 2 hours before CTA. No additional β-blocker was used when HR was >65 beats/min at the time of imaging. No patient had contraindications for β-blockers, and no β-blocker side effects were observed or reported. All patients received 2.5 mg of sublingual isosorbide dinitrate (Nitorol; Eisai, Tokyo, Japan) before imaging.

For each patient, the phase with minimum artifacts was determined at the CT console with the use of cardiac-phase search software (PhaseNavi; Toshiba Medical Systems Corporation, Tochigi, Japan). The reconstructed slice thickness was 0.50 mm, and the increment was 0.25 mm. Reconstruction was performed with data from a single heartbeat when the scan was acquired from a single heartbeat. When 2 or more beats were used for scanning, multicycle reconstruction was performed with data from multiple heartbeats, unless an ectopic heartbeat was detected or the patient could not stop breathing. Images in group 1 were reconstructed with FBP only, and images in group 2 were reconstructed with FBP and AIDR without changing the other reconstruction parameters such as field of view. We reconstructed images in group 2 with the use of FBP to investigate whether the difference of FBP and AIDR influences the CT number (in Hounsfield unit) of coronary arteries within the same patient. AIDR has 4 algorithm types, weak, moderate, standard, or strong, according to an increased number of iterations. The strong AIDR algorithm allows a maximum of 50% noise reduction. We used a strong AIDR algorithm for AIDR reconstruction of patients in group 2. For processing, images were transformed to a workstation (ZIO Station System; Ziosoft, Tokyo, Japan).

Subjective image analysis

Subjective image quality was rated by 2 cardiovascular readers (N.T. and T.N.) with 4 and 10 years of coronary CTA experience, respectively. The analysis was performed in a series reconstructed with FBP in group 1 and a series reconstructed with AIDR in group 2. The readers were not blinded from the reconstruction technique. This was because the texture of the AIDR image is somewhat different from the FBP image, and it was difficult to be completely blinded to the reconstruction technique. The American Heart Association 15-segment classification was applied for analysis of coronary angiography data.[12] The intermedial artery, when present, was designated as segment 16. Diagnostic study quality was graded on a per-artery level, and a study was deemed diagnostic when every anatomically present segment (≥1.5 mm) could be assessed for the presence of atherosclerosis and severity of stenosis. The results were scored according to the following 4-point scale: 4, excellent, no artifact; 3, good, mild artifact; 2, acceptable, moderate artifact present, but images still interpretable; 1, unable to evaluate, severe artifact makes interpretation impossible. When scores differed between the 2 readers, the final score was determined by consensus.

Objective image analysis

For all series reconstructed with FBP in group 1 and AIDR in group 2, image noise and the CT number of the proximal coronary arteries were measured, and the SNR and contrast-to-noise ratio (CNR) were calculated, according to previously described methods.[4] The region of interests (ROIs) were

drawn within a single axial slice for objective image analysis. A single radiologist (N.T.) with 4 years of coronary CTA experience collected the values. Image noise was defined as the standard deviation of the CT number in the ROI, placed in the ascending aorta above the coronary ostia (N). The ROI was chosen to be as large as possible while carefully avoiding inclusion of the aortic wall to prevent partial volume effects. The CT number within the lumen of the proximal coronary arteries was measured by placing the ROI centrally in the right coronary artery and left main trunk (A_V) and making the ROI as large as possible without including the coronary vessel wall. The CT number in the connective tissue was measured by placing the ROI immediately next to the vessel contour (A_C). SNR was calculated as A_V/N, and CNR was calculated as $(A_V - A_C)/N$. To compare the difference in CT number of the coronary arteries reconstructed with FBP and AIDR in 1 patient, the CT number in the left main trunk was measured for the series reconstructed with the use of FBP in group 2.

Statistical analysis

All statistical analyses were performed with JMP software (version 9.0.0; SAS Institute, Cary, NC). Quantitative variables are expressed as means ± SDs, unless otherwise described. Student *t* test was used to compare differences in age, BW, body mass index, HR, injection rate, tube current, and scan length. Fisher exact test was used to compare differences in sex, use of β-blockers, and heartbeats used for acquisition. The significance level of patient demographics and scan parameters was adjusted by the Bonferroni method, to 0.05/10 = 0.005.

Differences in the DLP of overall patients and with BW subgroups were assessed with the Mann-Whitney *U* test. The significance level was adjusted by the Bonferroni method to 0.05/6 = 0.008.

Interobserver agreement for image quality was calculated with Cohen κ statistic,[13] which was interpreted as poor (κ < 0.20), fair (κ = 0.21−0.40), moderate (κ = 0.41−0.60), good (κ = 0.61−0.80), very good (κ = 0.81−0.90), or excellent (κ ≥ 0.91).

Differences in subjective image quality scores were assessed with the Mann-Whitney *U* test. A *P* value < 0.05 was deemed to indicate significance. Differences in objective image quality (image noise, CT number, contrast, SNR, and CNR) were assessed with the Student *t* test. The significance level was adjusted by the Bonferroni method, to 0.05/9 = 0.0056. Differences in the CT number of the left main trunk between the FBP and AIDR reconstructions in group 2 were assessed with the Student *t* test. A *P* value of < 0.05 was deemed to indicate significance.

Results

Scanning parameters and radiation dose

HR, body mass index, injection rate, heartbeats used for acquisition, and scan length did not differ between the 2 groups. The average tube current was reduced by 40% in group 2 compared with group 1, reducing the overall median dose in group 2 (303 mGy · cm, 4.2 mSv) to 78% of the dose in group 1 (389 mGy · cm, 5.4 mSv) (Table 2). Analysis between BW subgroups showed a significant dose reduction in the 60- to 69-kg subgroup, although no significant difference was observed in the other subgroups. The median radiation dose of the 70- to 79-kg and 80- to 89-kg subgroups rose in group 2 compared with group 1 despite the use of lower tube current. This was because the proportion of multiple beat acquisition was higher in group 2 (70−79 kg, 6 of 9 patients; 80−89 kg, 2 of 2 patients) than in group 1 (70−79 kg, 4 of 11 patients; 80−89 kg, 1 of 3 patients). The radiation dose of the patient in the 90- to 99-kg subgroup in group 2 was about half the median radiation dose of the 80- to 89-kg subgroup because this patient was acquired from a single heartbeat.

Image quality

Interobserver agreement on subjective image quality was interpreted as "good" for both groups (κ = 0.73 for

Table 2 Dose length product

	Group 1		Group 2		
Parameter	No.	Median (interquartile range)	No.	Median (interquartile range)	*P*
Overall		389 (311−816)		303 (137−461)	0.0001*
BW					
<50 kg	7	484 (133−587)	5	333 (213−344)	0.74
50−59 kg	11	314 (293−731)	15	156 (120−380)	0.015
60−69 kg	18	375 (319−1035)	18	179 (125−397)	0.006*
70−79 kg	11	411 (346−1284)	9	576 (269−640)	0.36
80−89 kg	3	538 (389−1431)	2	703 (659−748)	0.77
90−99 kg	0	NA	1	310	NA

BW, body weight; NA, not applicable.
*The significance level was adjusted by the Bonferroni method to $P < 0.008$.

group 1 and 0.70 for group 2). Among 800 total segments, 93 and 125 segments in groups 1 and 2, respectively, were considered to be nonevaluable because the segment was absent (79 and 91 segments, respectively), too small (diameter, <1.5 mm; 13 and 30 segments, respectively), or completely occluded (1 and 4 segments, respectively). For group 1, 375 segments (53%) were scored as 4, 281 segments (40%) as 3, 36 segments (5%) as 2, and 15 segments (2%) as 1. For group 2, 383 segments (57%) were scored as 4, 255 segments (38%) as 3, 23 segments (3%) as 2, and 14 segments (2%) as 1. Although no significant difference was observed in subjective image quality between the 2 groups ($P = 0.12$), the proportion of segments with excellent (score 4) and good (score 3) image quality was higher in group 2 than in group 1 (Fig. 1).

The results of objective image quality are described in Table 3. The CT number and contrast were higher in group 2 reconstructed with AIDR than in group 1 reconstructed with FBP, and the differences were significant for the right coronary artery (Table 3). The CT number in the left main trunk was not significantly different between the FBP and AIDR reconstructions in group 2 (454.0 ± 92.0 HU and 453.4 ± 92.0 HU, respectively; $P = 0.97$). The noise in the aorta and the SNR and CNR in the right coronary artery and left main trunk did not differ significantly between the 2 groups.

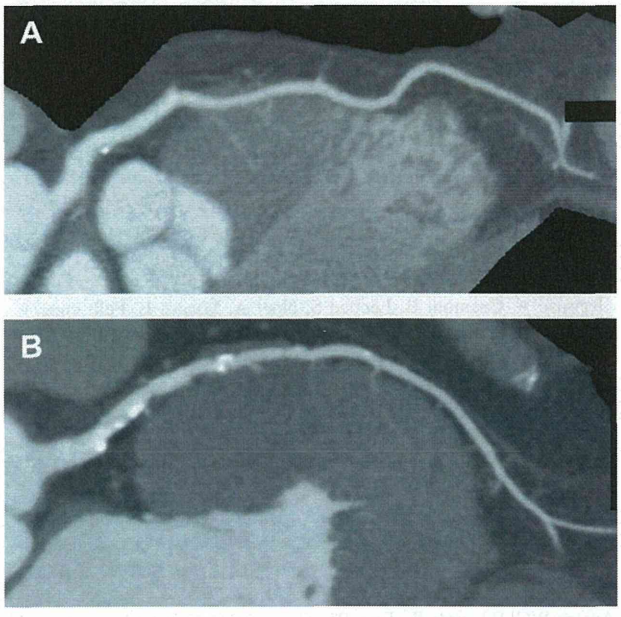

Figure 1 (**A**) Curved multiplanar reformat of the left anterior descending artery of a 67-year-old man with a body mass index of 24.5. The tube current was 500 mA and was reconstructed with filtered back projection. (**B**) Curved multiplanar reformat of the left anterior descending artery of a 78-year-old man with a body mass index of 25.1. The tube current was 270 mA and was reconstructed using Adaptive Iterative Dose Reduction. Note that the image quality of panel B is comparable with panel A despite the use of a 46% reduced tube current in panel B.

Table 3 Objective image quality

Parameter	Group 1 (FBP)	Group 2 (AIDR)	*P*
Aorta noise (HU)	22.1 ± 4.3	23.0 ± 4.0	0.30
RCA CT number (HU)	405.5 ± 66.6	447.0 ± 76.5	0.0047*
RCA contrast (HU)	474.4 ± 67.2	516.6 ± 70.3	0.0028*
RCA SNR	18.9 ± 4.6	19.9 ± 4.5	0.31
RCA CNR	22.1 ± 4.9	23.0 ± 4.7	0.38
LMT CT number (HU)	413.4 ± 66.0	453.4 ± 92.0	0.014
LMT contrast (HU)	486.3 ± 66.0	523.4 ± 92.0	0.023
LMT SNR	19.3 ± 5.0	20.2 ± 5.1	0.41
LMT CNR	22.8 ± 5.4	23.3 ± 5.4	0.62

AIDR, adaptive iterative dose reduction; CNR, contrast-to-noise ratio; FBP, filtered back projection; LMT, left main trunk; RCA, right coronary artery; SNR, signal-to-noise ratio.

*The significance level was adjusted by the Bonferroni method to $P < 0.0056$.

Discussion

Our study showed that coronary CTA with the use of an iterative reconstruction algorithm with a lower radiation dose maintained the subjective and objective image quality as using a FBP algorithm. The use of a decreased tube current and subsequently decreased number of photons would lead to an increase in image noise. The iterative reconstruction algorithm selectively identifies and subtracts image noise with every cycle of iteration. This process is repeated after each correction and regularization, which results in reducing noise while preserving image quality.[6] Importantly, one of the main advantages of iterative reconstruction techniques is that it is supplemental to other radiation dose reduction techniques.

The image noise was slightly higher in the AIDR group than in the FBP group because the dose reduction was higher in the 60- to 69-kg subgroup compared with other BW subgroups. This is because we ought to use a small focal spot size in this subgroup, and the maximum tube current for small focal spot size was 270 mA. We hypothesized that, although a small focal spot size produces a noisy image, it improves spatial resolution and results in a sharp image while maintaining diagnostic image quality.[14] Our results showed that, even though the image noise was slightly higher in the AIDR group than in the FBP group, the subjective image quality was slightly better in the AIDR group. Further study is necessary to determine in which patients a small focal spot size would be appropriate. The higher CT number in the AIDR group compared with the FBP group may also be attributable to the use of a small focal spot size, given that the CT number within the same patient reconstructed with FBP and AIDR was unchanged.

The reduction in tube current differed between BW subgroups. The tube current reduction was higher in

the 50- to 59- kg and 60- to 69-kg subgroups and lower in obese patients. The maximum tube current was 550 mA for this scanner, and this resulted in a noisy image in obese patients of the FBP group. To maintain good image quality for diagnosis, excessive dose reduction would not be appropriate in obese patients of the AIDR group.

The overall median radiation dose with the use of AIDR was 4.2 mSv, which is higher than that in previous studies that used an iterative reconstruction algorithm (2.0−3.2 mSv).[3,5,15,16] One of the reasons is that we used 120 kV for all patients, whereas 100 kV[3,15] or 80 kV[5] are used for thinner patients in previous studies. Another reason could be that the fastest gantry rotation time of this study was 350−400 milliseconds, which is slower than the previous studies (280−350 milliseconds).[3,5,15,16] In addition, the average HR was higher in the current study than in previous studies, making acquisition from multiple heartbeats necessary. Decreasing the HR with β-blockers at the time of the examination should help to lower the radiation dose. However, β-blockers influence ventricular function analysis[17,18] and are not recommended in CT for this purpose. In one study, even when β-blockers were used, 20%−30% of patients did not achieve the target HR.[19] Iterative reconstruction techniques would help to reduce the radiation dose in patients with high HRs.

Leipsic et al[3] showed that adaptive statistical iterative reconstruction (ASIR; GE Healthcare) allowed a lower median radiation dose, representing a 44% reduction, compared with FBP reconstruction. The interpretability of the coronary arteries did not differ between the FBP and ASIR images. Another study[16] achieved a 54% reduction in median radiation dose with the use of ASIR compared with FBP. Moscariello et al[5] showed lower image noise and slightly higher image quality in half-dose iterative reconstruction with sonogram-affirmed iterative reconstruction (SAFIRE; Siemens Healthcare) compared with full-dose FBP. The degree of radiation dose reduction with AIDR is comparable with these results. Bittencourt et al[4] reported a 20% noise reduction with the use of IRIS. Given that tube current reduction is related to the square of noise reduction, this reduction in noise should theoretically allow for a tube current reduction of approximately 30%, which is comparable with the results above.

Our study possessed several limitations. First, we did not test the diagnostic accuracy with coronary catheterization correlation. The aim of this study was to evaluate the image quality between the different reconstruction methods. With slightly better subjective image quality with the use of AIDR, the diagnostic accuracy may improve with AIDR. Second, we did not evaluate the image quality with other AIDR reconstruction methods such as weak, moderate, and standard AIDR. Third, the effect of using a small focal spot was not assessed in this study. Fourth, although the knowledge of the reconstruction technique may introduce bias, the use of objective image analysis should minimize that potential bias.

Conclusions

With the use of AIDR for reconstruction, coronary CTA performed with an average of 40% reduced tube current which resulted in 22% reduction in median radiation dose can maintain subjective and objective image quality compared with coronary CTA reconstructed with the use of FBP.

References

1. West AM, Beller GA: 256- and 320-row coronary CTA: is more better? Eur Heart J. 2010;31:1823–5.
2. Halliburton SS, Abbara S, Chen MY, Gentry R, Mahesh M, Raff GL, Shaw LJ, Hausleiter J: SCCT guidelines on radiation dose and dose-optimization strategies in cardiovascular CT. J Cardiovasc Comput Tomogr. 2011;5:198–224.
3. Leipsic J, LaBounty TM, Heilbron B, Min JK, Mancini GBJ, Lin FY, Taylor C, Dunning A, Earls JP: Estimated radiation dose reduction using adaptive statistical iterative reconstruction in coronary CT angiography: the ERASIR study. AJR Am J Roentgenol. 2010;195: 655–60.
4. Bittencourt MS, Bernhard Schmidt B, Seltmann M, Muschiol G, Ropers D, Daniel WG, Achenbach S: Iterative reconstruction in image space (IRIS) in cardiac computed tomography: initial experience. Int J Cardiovasc Imaging. 2011;27:1081–7.
5. Moscariello A, Takx RA, Schoepf UJ, Renker M, Zwerner PL, O'Brien TX, Allmendinger T, Vogt S, Schmidt B, Savino G, Fink C, Bonomo L, Henzler T: Coronary CT angiography: image quality, diagnostic accuracy, and potential for radiation dose reduction using a novel iterative image reconstruction technique—comparison with traditional filtered back projection. Eur Radiol. 2011;21:2130–8.
6. Nelson RC, Feuerlein S, Boll DT: New iterative reconstruction techniques for cardiovascular computed tomography: How do they work, and what are the advantages and disadvantages? J Cardiovasc Comput Tomogr. 2011;5:286–92.
7. Thibault J, Sauer KD, Bouman CA, Hsieh J: A three-dimensional statistical approach to improved image quality for multislice helical CT. Med Phys. 2007;34:4526–44.
8. Lrwan A, VerJooij C, Joemai R, Nanne R: AEC comparison with and without iterative dose reduction technique: a phantom study: Toshiba Medical Systems Journals. VISIONS. 2011;17:14–6.
9. Gervaise A, Osemont B, Lecocq S, Noel A, Micard E, Felblinger J, Blum A: CT image quality improvement using adaptive iterative dose reduction with wide-volume acquisition on 320-detector CT. Eur Radiol. 2012;22:295–301.
10. Hausleiter J, Meyer T, Hermann F, Hadamitzky M, Krebs M, Gerber TC, McCollough C, Martinoff S, Kasaatrati A, Schömig A, Achenbach S: Estimated radiation dose associated with cardiac CT angiography. JAMA. 2009;301:500–7.
11. Tomizawa N, Komatsu S, Akahane M, Torigoe R, Kiryu S, Ohtomo K: Influence of hemodynamic parameters on coronary artery attenuation with 320-detector coronary CT angiography. Eur J Radiol. 2012;81: 230–3.
12. Austen WG, Edwards JE, Frye RL, Gensini GG, Gott VL, Griffith LS, McGoon DC, Murphy ML, Roe BB: A reporting system on patients evaluated for coronary artery disease. Report of the Ad Hoc Committee for Grading of Coronary Artery Disease, Council on Cardiovascular Surgery, American Heart Association. Circulation. 1975;51:5–40.
13. Cohen J: A coefficient of agreement for nominal scales. Educ Psychol Meas. 1960;20:37–46.
14. Ishii T, Araki I, Kyuba K, Kimijima S, Sugisawa K, Shoji T, Hasegawa H: Knowledge and technique for cardiac CT [Article in Japanese]. Japanese J Radiol Tech. 2011;67:549–64.

15. Leipsic J, LaBounty TM, Heilbron B, Min JK, Mancini GBJ, Lin FY, Taylor C, Dunning A, Earls JP: Adaptive statistical iterative reconstruction: assessment of image noise and image quality in coronary CT angiography. AJR Am J Roentgenol. 2010;195:649–54.
16. Gosling O, Loader R, Venables P, Roobottom C, Rowles N, Bellenger N, Morgan-Hughes G: A comparison of radiation doses between state-of-the-art multislice CT coronary angiography with iterative reconstruction, multislice CT coronary angiography with standard filtered back-projection and invasive diagnostic coronary angiography. Heart. 2010;96:922–6.
17. Mahabadi AA, Achenbach S, Burgstahler C, Dill T, Fischbach R, Knez A, Moshage W, Richartz BM, Ropers D, Schröder S, Silber S, Möhlenkamp S: Safety, efficacy, and indications of β-adrenergic receptor blockade to reduce heart rate prior to coronary CT angiography. Radiology. 2010;257:614–23.
18. Jensen CJ, Jochims M, Hunold P, Forsting M, Barkhausen J, Sabin GV, Bruder O, Schlosser T: Assessment of left ventricular function and mass in dual-source computed tomography coronary angiography. Influence of beta-blockers on left ventricular function: Comparison to magnetic resonance imaging. Eur J Radiol. 2010;74:484–91.
19. de Graaf FR, Schuijf JD, van Velzen JE, Kroft LJ, de Roos A, Sieders A, Jukema JW, Schalij MJ, van der Wall EE, Bax JJ: Evaluation of contraindications and efficacy of oral beta blockade before computed tomographic coronary angiography. Am J Cardiol. 2010;105:767–72.

Connective Tissue Research, 2012; 53(5): 349–354

ISSN: 0300-8207 print/1607-8438 online
DOI: 10.3109/03008207.2012.657309

informa
healthcare

Differential Expression of Wound Fibrotic Factors between Facial and Trunk Dermal Fibroblasts

Masakazu Kurita,[1] Mutsumi Okazaki,[2] Akiko Kaminishi-Tanikawa,[1] Mamoru Niikura,[3] Akihiko Takushima,[1] Kiyonori Harii[1]

[1]*Department of Plastic Surgery, Kyorin University School of Medicine, Tokyo, Japan,* [2]*Department of Plastic and Reconstructive Surgery, Graduate School, Tokyo Medical and Dental University, Tokyo, Japan,* [3]*Department of Parasitology, Kyorin University School of Medicine, Tokyo, Japan*

Clinically, wounds on the face tend to heal with less scarring than those on the trunk, but the causes of this difference have not been clarified. Fibroblasts obtained from different parts of the body are known to show different properties. To investigate whether the characteristic properties of facial and trunk wound healing are caused by differences in local fibroblasts, we comparatively analyzed the functional properties of superficial and deep dermal fibroblasts obtained from the facial and trunk skin of seven individuals, with an emphasis on tendency for fibrosis. Proliferation kinetics and mRNA and protein expression of 11 fibrosis-associated factors were investigated. The proliferation kinetics of facial and trunk fibroblasts were identical, but the expression and production levels of profibrotic factors, such as extracellular matrix, transforming growth factor-β1, and connective tissue growth factor mRNA, were lower in facial fibroblasts when compared with trunk fibroblasts, while the expression of antifibrotic factors, such as collagenase, basic fibroblast growth factor, and hepatocyte growth factor, showed no clear trends. The differences in functional properties of facial and trunk dermal fibroblasts were consistent with the clinical tendencies of healing of facial and trunk wounds. Thus, the differences between facial and trunk scarring are at least partly related to the intrinsic nature of the local dermal fibroblasts.

Keywords: fibrosis, scarring, fibroblast, heterogeneity, tissue specificity

Introduction

Fibroblasts are the most common cells present in connective tissues, where they synthesize extracellular matrix (ECM) and play a critical role in wound healing [1]. Fibroblasts are known to be composed of diverse cell populations and manifest phenotypic differences in their function, such as ECM production and organization, and production of growth factors and cytokines [2–5]. These differences in properties are notable in cutaneous pathological conditions such as keloid [6], hypertrophic scar [7], scleroderma [8], café au lait macule [9], and neurofibroma [10], and even under physiological conditions, fibroblasts exhibit differences; this is known as fibroblast heterogeneity [3–5]. The functional differences are particularly evident between superficial dermal fibroblasts and deep dermal fibroblasts [3–5,11–15]. Heterogeneity also exists between anatomical locations, as several recent studies have indicated that fibroblasts from different body sites retain positional information and topographic differentiation patterns in the expression of genes in vitro [16,17]. However, there are limited reports of the differences in wound healing-associated functions between dermal fibroblasts based on body sites [18].

Clinically, wounds on the face and trunk show different tendencies for wound scarring [19]. Facial incisional wounds, particularly preauricular incisional wounds, heal with less scarring than similar wounds on the trunk. Factors such as the innate properties of resident cells, thickness and compositional structure of the dermis, perfusing blood flow, and mechanical stresses such as skin tension are thought to be the reasons for such differences [19,20]. However, to our knowledge, no studies have elucidated the specific mechanisms responsible.

In order to clarify whether the characteristic properties of facial and trunk scarring are due to differences in local fibroblasts, functional differences between facial dermal fibroblasts and trunk dermal fibroblasts were investigated, using primary facial superficial dermal fibroblasts (FS), facial deep dermal fibroblasts (FD), trunk superficial dermal fibroblasts (TS), and trunk deep dermal fibroblasts (TD). Thus, cellular proliferation kinetics, and expression and production of 11 fibrosis-associated factors, including representative ECM metabolism-associated factors or cytokines, which are considered to be related to scar fibrosis, were investigated and compared between facial and trunk dermal fibroblasts.

Materials and Methods

Cell Isolation and Culture

Facial (preauricular) and trunk (lateral thoracic) skin was obtained during reconstructive surgery from seven healthy donors without antecedent operative invasion to the biopsied site (four females and three males; age, 46.6 ± 14.4 years). Profiles and data description codes are shown in Table 1. The research protocol was approved by the internal review board of our university hospital. Informed consent was obtained from all patients. After resection of subcutaneous tissues, specimens were washed three times in phosphate-buffered saline, and the external and internal surfaces were dermatomed in order to obtain superficial and deep dermal samples, respectively. To avoid cellular selection bias, both

Address correspondence to Masakazu Kurita, MD, PhD, Department of Plastic Surgery, Kyorin University School of Medicine, 6-20-2 Shinkawa, Mitaka-shi, Tokyo 181-8611, Japan. Tel.: +81-422-47-5511; Fax: +81-422-46-0138. E-mail: masakazukurita@aol.com
Received 31 October 2011; Revised 9 January 2012; Accepted 10 January 2012

Table 1. Profiles and data description codes of samples

No.	Age	Sex	Proliferation assay	Real-time PCR assay	ELISA (collagen I)	ELISA (cytokines)	Symbol in figures
1	44	M	*	*	*	*	○
2	34	M	*	*	*	*	△
3	60	F	*	*	*	*	□
4	65	M	*	*	*	*	•
5	53	F	*	*	*	*	▲
6	24	F	*	*		*	■
7	46	F	*	*			×

samples were incubated with 0.25% trypsin and 0.02% EDTA in phosphate-buffered saline for 16–24 hr at 4°C and the epithelium was separated from the superficial dermal sample. From the separated superficial and deep dermal samples, human fibroblasts were cultured as explants and maintained at 37°C under a 5% CO_2 atmosphere in fibroblast growth medium (FGM) consisting of Dulbecco's modified Eagle's medium (DMEM) supplemented with 10% fetal calf serum and 0.6 mg/ml glutamine. After about 3 weeks, primary cultures were subcultured. Medium was replaced every 3 days during cell culture.

Proliferation Assay

Cells at the third passage were plated in triplicate in 12-well plates at 1.0×10^4 cells/well in FGM. Medium was replaced every 4 days and the cell number was manually counted at the same time until day 32.

Quantification of mRNA by Real-Time Polymerase Chain Reaction

Cells at four or five passages were plated in 12-well plates at 1.0×10^4 cells/well in FGM. On day 4, total RNA was isolated using an RNeasy™ Mini Kit and QIA shredder (both from QIAGEN, Hilden, Germany), followed by reverse transcription using a High Capacity RNA-to-cDNA kit. Wound maturation-associated genes (listed in Table 2) were quantified using real-time polymerase chain reaction (PCR). Reaction mixtures comprised 10 µl of FAST SYBR® Green Master Mix and 1 µl of cDNA sample and RNase-free water with the indicated primer concentrations. Reactions were performed and monitored using the StepOnePlus™ real-time PCR system. All PCR reagents and the PCR system were obtained from Applied Biosystems (Foster City, CA, USA). PCR comprised 40 cycles, consisting of denaturing at 95°C (3 s) and annealing/extension at 60°C (15 s). Primer sequences were designed based on previous studies and were optimized for concentration [8,21–25]. Primers for which amplification efficiency was between 1.95 and 2.05 were employed for the study. Sequences and optimized concentrations for each primer are shown in Table 2. For quantification, expression levels were calculated by the comparative CT method using glyceraldehyde-3-phosphate dehydrogenase (GAPDH) and human acidic ribosomal protein (HARP) as an endogenous reference gene. Preliminary tests confirmed that both the endogenous controls offered similar results. Therefore, we decided to use GAPDH as an internal control throughout the study.

Measurement of ECM and Cytokines by Enzyme-Linked Immunesorbent Assay

Samples for enzyme-linked immunesorbent assay (ELISA) were collected under the same culture conditions as cDNA. Soluble and sediment type I collagens were quantitatively analyzed by ELISA (Human collagen I EIA kit; Applied Cell Biotechnologies, Inc., Yokohama, Kanagawa, Japan) according to the manufacturer's instructions. Transforming growth factor-β1 (TGF-β1), transforming growth factor-β2 (TGF-β2), and connective tissue growth factor (CTGF) in culture supernatants were also measured by ELISA (Quantikine™ from R&D Systems (Minneapolis, MN, USA) for TGF-β1 and TGF-β2, and Human CTGF ELISA Kit from Cusabio, Inc., Wuhan, Hubei, China, for CTGF), in accordance with the manufacturer's instructions. Levels of each factor were measured using a microplate reader (Power Scan® HT; Dainippon Pharmaceutical, Osaka, Japan). Data are expressed as secreted factors per 1.0×10^4 cells at the time of harvest.

Statistical Analyses

Differences in values between groups of cells were analyzed by paired Student's *t*-test. In the proliferation assay, associations between cell number of facial dermal fibroblasts and trunk dermal fibroblasts at confluence (on day 32) were statistically analyzed using Pearson's correlation index. Values of $p < 0.05$ were considered to be statistically significant. Chronological changes in cell number are presented as means ± standard error of the mean, and other data are presented as means ± standard deviation.

Results

Cell Morphology and Proliferation

Morphologically, no differences were observed between dermal fibroblasts obtained from the face and trunk, while superficial dermal fibroblasts and deep dermal fibroblasts showed apparent differences regardless of donor site. Superficial dermal fibroblasts were smaller and spindle-shaped when compared with deep dermal fibroblasts, which tended to broadly spread on the surface (Figure 1). In addition, with regard to proliferation kinetics, no differences were observed between facial and trunk dermal fibroblasts, although the cellular density of superficial dermal fibroblasts tended to be higher than that of deep dermal fibroblasts on proliferation assay (Figure 2A), as shown in the comparative description of cell numbers of FS, FD, TS, and TD on day 32 (Figure 2B). Cell numbers at confluency on day 32 demonstrated that for superficial dermal fibroblasts and deep dermal fibroblasts, respectively, cellular density of facial and trunk dermal fibroblasts from the same donor showed significant correlations (Figure 2C).

mRNA Expression of Fibrosis-Associated Factors

In order to investigate the functional differences between facial and trunk dermal fibroblasts, mRNA expression of fibrosis-associated factors in superficial dermal fibroblasts and deep dermal fibroblasts was quantitatively compared using real-time PCR.

Among superficial dermal fibroblasts, FS showed lower expression of ECMs such as type I and III collagens, fibronectin, TGF-β1 and TGF-β3, and CTGF when compared with TS. On the other

Table 2. Primer sequences and optimized concentrations for real-time PCR

Gene	Coding protein	Sequence	Primer concentration [nM]
COL1A1	Type I collagen	F: CCCACCAATCACCTGCGTACAGA	100
		R: TTCTTGGTCGGTGGGTGACTCTGA	100
COL3A1	Type III collagen	F: GAGATGTCTGGAAGCCAGAACCAT	100
		R: GATCTCCCTTGGGGCCTTGAGGT	100
FN1	Fibronectin	F: GGAGAATTCAAGTGTGACCCTCA	300
		R: TGCCACTGTTCTCCTACGTGG	300
MMP1	MMP1 (collagenase)	F: TCTGGGGTGTGGTGTCTCA	300
		R: GCCTCCCATCATTCTTCAGGTT	300
TGFB1	TGF-β1	F: GTTCAAGCAGAGTACACACAGC	300
		R: GTATTTCTGGTACAGCTCCACG	300
TGFB2	TGF-β2	F: ATGCGGCCTATTGCTTTAGA	200
		R: TAAGCTCAGGACCCTGCTGT	200
TGFB3	TGF-β3	F: CAGGGAGAAAATCCAGGTCA	100
		R: CCTGGAAGGCGTCTAACCAAG	100
CTGF	CTGF	F: ACGGCGAGGTCATGAAGAAGAACA	100
		R: ACTCTCTGGCTTCATGCCATGTCT	100
ASMA	α-smooth muscle actin	F: CCAAGCACTGTCAGGAAT	100
		R: AGGCAGTGCTGTCCTCTT	100
FGF2	bFGF	F: ATACAGCAGCAGCCTAGCAACTCT	100
		R: TTCGGCAACAGCACACAAATCCTG	100
HGF	HGF	F: GCAAGTGAATGGAAGTCCTTTA	100
		R: CAGAGGGACAAAGGAAAAGAA	100
SCF	SCF	F: GCCGCTGTTCGTGCAATAT	200
		R: CTGCGATCCAGCACAAACAGT	200
HARP	HARP	F: CGCTGCTGAACATGCTCAA	300
		R: TGTCGAACACCTGCTGGATG	300
GAPDH	GAPDH	F: GAAGGTGAAGGTCGGAGTC	300
		R: GAAGATGGTGATGGGATTTC	300

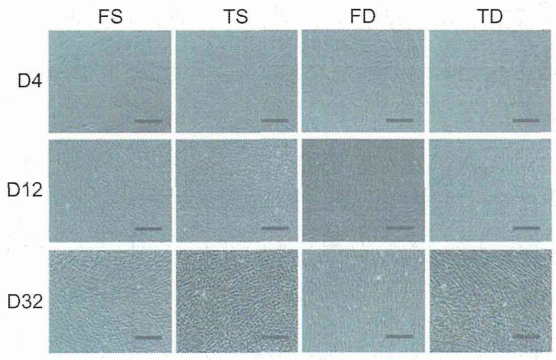

Figure 1. Cell morphology of FS, TS, FD, and TD. Phase contrast microscopic findings for FS, TS, FD, and TD from donor No. 4 at 4, 12, and 32 days after cell seeding. Scale bar indicates 100 μm.

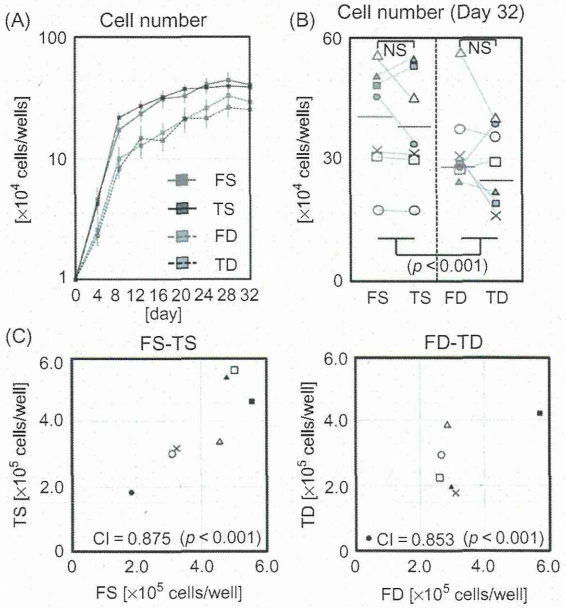

Figure 2. Cell proliferation of FS, TS, FD, and TD. (A) Chronological cell number in four cell fractions is noted ($n = 7$ for each). Error bars indicate SEM. (B) Cell count of FS, TS, FD, and TD on day 32 ($n = 7$ for each). (C) Correlation of saturated cell number between facial and trunk fibroblasts on day 32.

hand, expression of TGF-β2 was higher in FS than in TS. Expression of MMP1, ASMA, bFGF, and HGF showed no clear trends. Among deep dermal fibroblasts, FD showed lower expression of TGF-β1 and CTGF than TD, while no clear trends were seen for other factors (Figure 3).

Production of Fibrosis-Associated Factors

In order to further confirm the differences between facial and trunk dermal fibroblasts, protein production of type I collagen, TGF-β1, TGF-β2, and CTGF were compared by ELISA.

Among superficial dermal fibroblasts, FS showed significantly lower production of type I collagen, TGF-β1, and CTGF than TS. this was consistent with the results of mRNA expression analysis. In addition, production of TGF-β2 showed the same trend as for mRNA expression, with higher production in FS than that in TS, although the differences were not significant. Among deep dermal fibroblasts, similar to results of mRNA expression analysis, FD showed lower production of TGF-β1 and CTGF than TD, and no clear trends were seen for type I collagen and TGF-β2 (Figure 4).

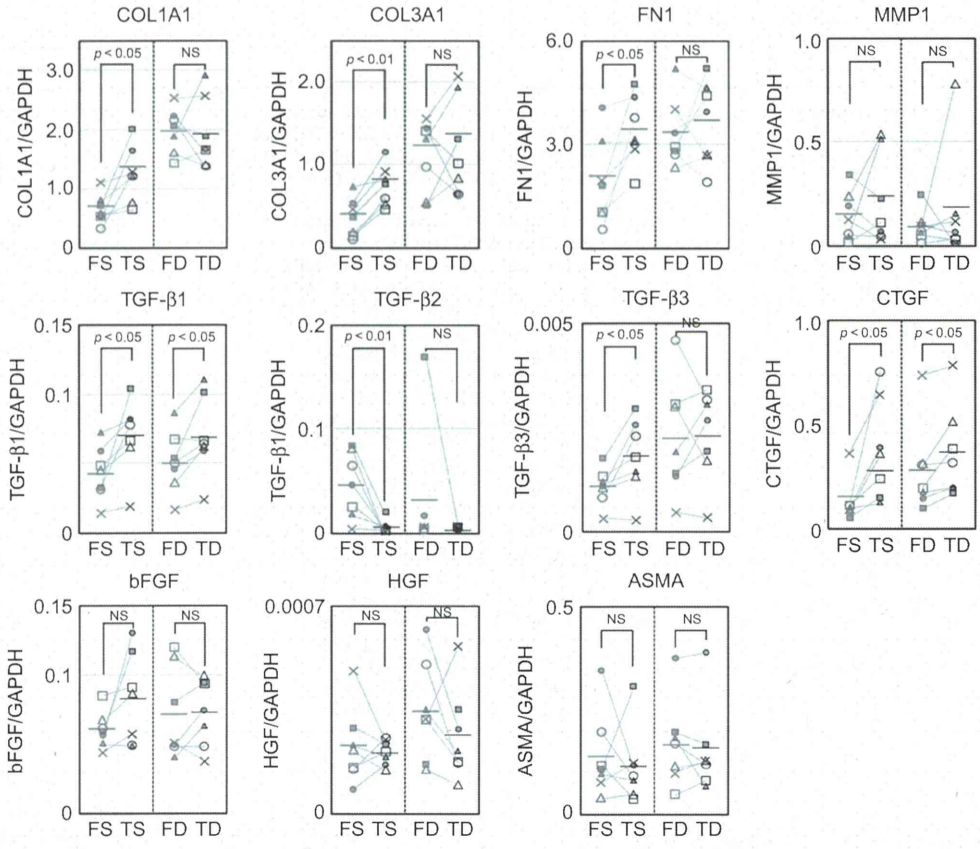

Figure 3. Expression of wound healing-associated factors by FS, TS, FD, and TD. mRNA expression of fibrosis-associated factors by FS, FD, TS, and TD ($n = 7$, each).

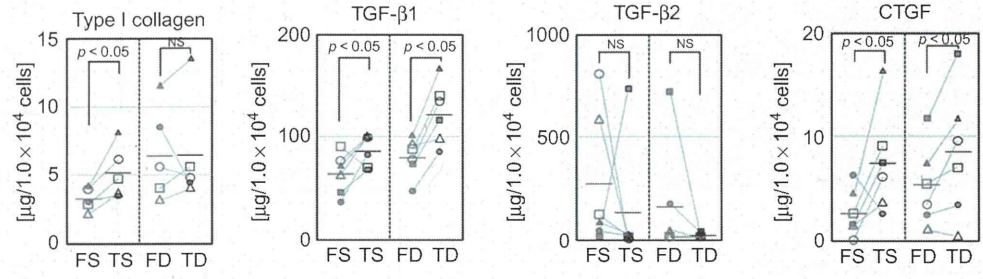

Figure 4. Production of wound healing-associated factors by FS, TS, FD, and TD. Production of type I collagen, TGF-β1 and TGF-β2, and CTGF by FS, FD, TS, and TD (for type I collagen, $n = 5$ for each; for others, $n = 6$ for each).

Discussion

In our analysis of seven paired FS, FD, TS, and TD samples from the same individuals, facial and trunk dermal fibroblasts obtained from the same layers of dermis showed identical morphology and proliferation kinetics, while differences in depth of origin distinctly affected cell morphology and proliferation kinetics, as indicated in previous reports [11–15]. On the other hand, the cellular density of facial and trunk dermal fibroblasts from the same depth of dermis in the same individuals showed significant, positive correlations. The proliferative capability of superficial and deep dermal fibroblasts is thought not to be influenced by anatomical site, but is specific to donor individuals.

In a subsequent study, mRNA expression of 11 genes considered to be associated with scarring (i.e., fibrosis formation) was investigated between facial and trunk dermal fibroblasts. Type I and III collagens, fibronectin, and collagenase expression were investigated because ECM production causes excess deposition of ECM, and were considered to be a profibrotic factor [8,9,26], while collagenase expression is considered to be an antifibrotic factor [11,27]. Other cytokines, such as TGF-βs, CTGF, bFGF, and HGF, were also investigated because these may be involved in fibrotic processes [11,27–31]. TGF-β1 and its downstream mediator CTGF are known to play particular important roles in hypertrophic scar formation and keloids [6,12,24,30,32] and are therefore considered to be dominant profibrotic factors. TGF-β2

[19,31] and TGF-β3 [19,30,31,33,34] also play important roles in the process of fibrotic scar formation, although their relative dominance during scar development is smaller when compared with TGF-β1 and CTGF, and their effects on scarring were not clearly defined as pro- or antifibrotic. On the other hand, HGF is reported to have antifibrogenic effects in various organs [35,36], and much more recently, bFGF was found to prevent fibrogenesis via activation of HGF secretion from adipose-derived cells and dermal fibroblasts [37]. Therefore, we also investigated the expression of HGF and bFGF as possible antifibrotic factors.

Between facial and trunk dermal fibroblasts, differences in expression and/or production of fibrosis-associated factors have been noted. In particular, it was noted that expression and production of TGF-β1 and CTGF, known as one of the most potent fibrosis-inducing factors [6,12,24,30,32], were lower in facial fibroblasts than in trunk fibroblasts. Moreover, with regard to superficial dermal fibroblasts, facial fibroblasts showed lower expression and/or production of ECMs than trunk fibroblasts. This indicates that facial dermal fibroblasts are intrinsically less fibrotic than trunk dermal fibroblasts, although the reasons for the differences in TGF-β2 and TGF-β3 expressions in fibrosis are unclear.

Our study demonstrated that facial and trunk dermal fibroblasts in the superficial and deep dermis possess identical proliferative capacity, but that facial dermal fibroblasts show lower fibrotic activity in mRNA expression and protein production analyses. We believe that these functional differences in local dermal fibroblasts are at least partly responsible for the clinically observed differences in scarring in the face and trunk. (Facial wounds tend to heal with less scarring than trunk wounds.)

As noted by Chang et al. in a genome-wide mRNA expression analysis using a microarray, fibroblasts obtained from various body sites displayed distinct and characteristic transcriptional patterns, particularly with regard to HOX genes established during embryogenesis, and fibroblasts at different locations in the body should be considered as distinct differentiated cell types [16]. During the developmental process, the dermal component is generally derived from lateral plate mesoderm and somite [38], however, the dermis of the face and ventral neck area is specifically differentiated from neural crest cells via formation of mesoectoderm [38,39]. We believe that these developmental differences are the cause of the functional differences observed in our study. Future studies should aim to clarify more fundamental differences between facial and dermal fibroblasts, similar to the work of Yamaguchi et al., which revealed that the physiological differences in melanin pigment between palmoplantar and nonpalmoplantar skin are associated with elevated expression of dickkopf-1, an inhibitor of the canonical Wnt signaling pathway which is also associated with developmental processes [18]. Further clarification of key factors in the anatomical differences in the scarring properties of fibroblasts may contribute to future therapeutic intervention for problematic wound scarring, such as conspicuous scars resulting from excess scar formation, hypertrophic scarring, or keloids.

Conclusions

Our study demonstrated that facial and trunk dermal fibroblasts in the superficial and deep dermis possess identical proliferative capacity, but that facial dermal fibroblasts show lower fibrotic activity in mRNA expression and protein production analyses. The differences in functional properties of facial and trunk dermal fibroblasts were consistent with the clinical healing tendencies of facial and trunk wounds. Thus, the differences between facial and trunk scarring are, in part, related to the intrinsic nature of the local dermal fibroblasts.

Acknowledgment

This work was supported by a grant from the Japanese Ministry of Education, Culture, Sports, Science, and Technology (MEXT) KAKENHI 21689046 (Grant-in-Aid for Young Scientists A) and 20390457 (Grant-in-Aid for Scientific Research B).

Declaration of interest

The authors declare that they have no other competing financial interests.

References

1. Martin, P. (1997). Wound healing – Aiming for perfect skin regeneration. *Science.* 276:75–81.
2. Fries, K.M., Blieden, T., Looney, R.J., Sempowski, G.D., Silvera, M.R., Willis, R.A., and Phipps, R.P. (1994). Evidence of fibroblast heterogeneity and the role of fibroblast subpopulations in fibrosis. *Clin. Immunol. Immunopathol.* 72:283–292.
3. Sorrell, J.M., and Caplan, A.I. (2004). Fibroblast heterogeneity: More than skin deep. *J. Cell Sci.* 117:667–675.
4. Sorrell, J.M., Baber, M.A., and Caplan, A.I. (2004). Site-matched papillary and reticular human dermal fibroblasts differ in their release of specific growth factors/cytokines and in their interaction with keratinocytes. *J. Cell. Physiol.* 200:134–145.
5. Sorrell, J.M., Baber, M.A., and Caplan, A.I. (2008). Human dermal fibroblast subpopulations; differential interactions with vascular endothelial cells in coculture: Nonsoluble factors in the extracellular matrix influence interactions. *Wound Repair Regen.* 16:300–309.
6. Smith, J.C., Boone, B.E., Opalenik, S.R., Williams, S.M., and Russell, S.B. (2008). Gene profiling of keloid fibroblasts shows altered expression in multiple fibrosis-associated pathways. *J. Invest. Dermatol.* 128: 1298–1310.
7. Dasu, M.R., Hawkins, H.K., Barrow, R.E., Xue, H., and Herndon, D.N. (2004). Gene expression profiles from hypertrophic scar fibroblasts before and after IL-6 stimulation. *J. Pathol.* 202:476–485.
8. Jelaska, A., Arakawa, M., Broketa, G., and Korn, J.H. (1996). Heterogeneity of collagen synthesis in normal and systemic sclerosis skin fibroblasts. Increased proportion of high collagen-producing cells in systemic sclerosis fibroblasts. *Arthritis Rheum.* 39:1338–1346.
9. De Schepper, S., Boucneau, J., Vander Haeghen, Y., Messiaen, L., Naeyaert, J.M., and Lambert, J. (2006). Café-au-lait spots in neurofibromatosis type 1 and in healthy control individuals: Hyperpigmentation of a different kind? *Arch. Dermatol. Res.* 297:439–449.
10. Okazaki, M., Yoshimura, K., Suzuki, Y., Uchida, G., Kitano, Y., Harii, K., and Imokawa, G. (2003). The mechanism of epidermal hyperpigmentation in café-au-lait macules of neurofibromatosis type 1 (von Recklinghausen's disease) may be associated with dermal fibroblast-derived stem cell factor and hepatocyte growth factor. *Br. J. Dermatol.* 148:689–697.
11. Ali-Bahar, M., Bauer, B., Tredget, E.E., and Ghahary, A. (2004). Dermal fibroblasts from different layers of human skin are heterogeneous in expression of collagenase and types I and III procollagen mRNA. *Wound Repair Regen.* 12:175–182.
12. Wang, J., Dodd, C., Shankowsky, H.A., Scott, P.G., Tredget, E.E., and Wound Healing Research Group. (2008). Deep dermal fibroblasts contribute to hypertrophic scarring. *Lab. Invest.* 88:1278–1290.
13. Harper, R.A., and Grove, G. (1979). Human skin fibroblasts derived from papillary and reticular dermis: Differences in growth potential in vitro. *Science* 204:526–527.
14. Azzarone, B., and Macieira-Coelho, A. (1982). Heterogeneity of the kinetics of proliferation within human skin fibroblastic cell populations. *J. Cell. Sci* 57:177–187.
15. Schafer, I.A., Pandy, M., Ferguson, R., and Davis, B.R. (1985). Comparative observation of fibroblasts derived from the papillary and reticular dermis of infants and adults: Growth kinetics, packing density ant confluence and surface morphology. *Mech. Ageing Dev.* 31:275–293.
16. Chang, H.Y., Chi, J.T., Dudoit, S., Bondre, C., van de Rijn, M., Botstein, D., and Brown, P.O. (2002). Diversity, topographic differentiation, and positional memory in human fibroblasts. *Proc. Natl. Acad. Sci. USA* 99 (20):12877–12882.

17. Rinn, J.L., Bondre, C., Gladstone, H.B., Brown, P.O., and Chang, H.Y. (2006). Anatomic demarcation by positional variation in fibroblast gene expression programs. *PLoS Genet.* 2:e119.
18. Yamaguchi, Y., Passeron, T., Watabe, H., Yasumoto, K., Rouzaud, F., Hoashi, T., and Hearing, V.J. (2007). The effects of dickkopf 1 on gene expression and Wnt signaling by melanocytes: Mechanisms underlying its suppression of melanocyte function and proliferation. *J. Invest. Dermatol.* 127:1217–1225.
19. Ferguson, M.W., and O'Kane, S. (2004). Scar-free healing: From embryonic mechanisms to adult therapeutic intervention. *Philos. Trans. R. Soc. Lond. B Biol. Sci.* 359:839–850.
20. Gangemi, E.N., Gregori, D., Berchialla, P., Zingarelli, E., Cairo, M., Bollero, D., Ganem, J., Capocelli, R., Cuccuru, F., Cassano, P., Risso, D., and Stella, M. (2008). Epidemiology and risk factors for pathologic scarring after burn wounds. *Arch. Facial. Plast. Surg.* 10:93–102.
21. Thiele, B.J., Doller, A., Kähne, T., Pregla, R., Hetzer, R., and Regitz-Zagrosek, V. (2004). RNA-binding proteins heterogeneous nuclear ribonucleoprotein A1, E1, and K are involved in post-transcriptional control of collagen I and III synthesis. *Circ. Res.* 95:1058–1066.
22. Suga, H., Matsumoto, D., Eto, H., Inoue, K., Aoi, N., Kato, H., Araki, J., and Yoshimura, K. (2009). Functional implications of CD34 expression in human adipose-derived stem/progenitor cells. *Stem Cells Dev.* 18:1201–1210.
23. Goldberg, M.T., Han, Y.P., Yan, C., Shaw, M.C., and Garner, W.L. (2007). TNF-alpha suppresses alpha-smooth muscle actin expression in human dermal fibroblasts: An implication for abnormal wound healing. *J. Invest. Dermatol.* 127:2645–2655.
24. Pohlers, D., Beyer, A., Koczan, D., Wilhelm, T., Thiesen, H.J., and Kinne, R.W. (2007). Constitutive upregulation of the transforming growth factor-beta pathway in rheumatoid arthritis synovial fibroblasts. *Arthritis. Res. Ther.* 9:R59.
25. Quesnel, C., Marchand-Adam, S., Fabre, A., Marchal-Somme, J., Philip, I., Lasocki, S., Leçon, V., Crestani, B., and Dehoux, M. (2008). Regulation of hepatocyte growth factor secretion by fibroblasts in patients with acute lung injury. *Am. J. Physiol. Lung. Cell. Mol. Physiol.* 294:L334–L343.
26. Ala-Kokko, L., Rintala, A., and Savolainen, E.R. (1987). Collagen gene expression in keloid. Analysis of collagen metabolism and type I, III, IV and V procollagen mRNAs in keloid tissue and keloid fibroblast cultures. *J. Invest. Dermatol.* 89:238–244
27. Ghahary, A., Shen, Y.J., Nedelec, B., Wang, R., Scott, P.G., and Tredget, E.E. (1996). Collagenase production is lower in post-burn hypertrophic scar fibroblasts than normal fibroblasts and is down-regulated by insulin-like growth factor-1. *J. Invest. Dermatol.* 106:476–481.
28. Derynck, R., and Zhang, Y.E. (2003). Smad-dependent and Smad-independent pathways in TGF-β family signalling. *Nature* 425: 577–584.
29. Amjad, S.B., Carachi, R., and Edward, M. (2007). Keratinocyte regulation of TGF-beta and connective tissue growth factor expression: A role in suppression of scar tissue formation. *Wound Repair Regen.* 15: 748–755.
30. Barrientos, S., Stojadinovic, O., Golinko, M.S., Brem, H., and Tomic-Canic, M. (2008). Growth factors and cytokines in wound healing. *Wound Repair Regen.* 16:585–601.
31. Shah, M., Foreman, D.M., and Ferguson, M.W. (1995). Neutralisation of TGF-beta 1 and TGF-beta 2 or exogenous addition of TGF-beta 3 to cutaneous rat wounds reduces scarring. *J. Cell. Sci.* 108:985–1002.
32. Frazier, K., Williams, S., Kothapalli, D., Klapper, H., and Grotendorst, G.R. (1996). Stimulation of fibroblast cell growth, matrix production, and granulation tissue formation by connective tissue growth factor. *J. Invest. Dermatol.* 107:404–411.
33. Wu, L., Siddiqui, A., Morris, D.E., Cox, D.A., Roth, S.I., and Mustoe, T.A. (1997). Transforming growth factor beta 3 (TGF beta 3) accelerates wound healing without alteration of scar prominence. Histologic and competitive reverse-transcription polymerase chain reaction studies. *Arch. Surg.* 132:753–760.
34. Murata, H., Zhou, L., Ochoa, S., Hasan, A., Badiavas, E., and Falanga, V. (1997). F-beta3 stimulates and regulates collagen synthesis through TGF-beta1-dependent and independent mechanisms. *J. Invest. Dermatol.* 108:258–262.
35. Ueki, T., Kaneda, Y., Tsutsui, H., Nakanishi, K., Sawa, Y., Morishita, R., Matsumoto, K., Nakamura, T., Takahashi, H., Okamoto, E., and Fujimoto, J. (1999). Hepatocyte growth factor gene therapy of liver cirrhosis in rats. *Nat. Med.* 5:226–230.
36. Liu, Y. (2004). Hepatocyte growth factor in kidney fibrosis: Therapeutic potential and mechanisms of action. *Am. J. Physiol. Renal. Physiol.* 287:7–16.
37. Suga, H., Eto, H., Shigeura, T., Inoue, K., Aoi, N., Kato, H., Nishimura, S., Manabe, I., Gonda, K., and Yoshimura, K. (2009). S collection: Fibroblast growth factor-2-induced hepatocyte growth factor secretion by adipose-derived stromal cells inhibits postinjury fibrogenesis through a c-Jun N-terminal kinase-dependent mechanism. *Stem Cells* 27:238–249.
38. Sadler, T.W. (2009). *Langman's Medical Embryology*, 11th ed. Philadelphia: Lippincott Williams & Wilkins.
39. Nakamura, H. (1982). Mesenchymal derivatives from the neural crest. *Arch. Histol. Jpn.* 45:127–138.